

Building Bulk and Interface Dual Fast Li⁺ Conducting Pathway in Composite Solid Polymer Electrolyte Membrane for All-Solid-State Lithium–Metal Batteries

Yuanyuan He,^[a] Jiawen Tang,^[a] Xiao Huang,^[a] Xin Ao,*^[b] and Bingbing Tian*^[a]

Solid polymer electrolytes (SPEs) are considered a promising solution to the safety problems of lithium-ion batteries (LIBs) using liquid electrolytes. However, the high crystallinity and low ionic conductivity hinder the practical application of SPEs. Herein, we design a composite solid polymer electrolyte with a dual fast Li⁺ conducting pathway in bulk and interface by incorporating highly Li⁺ conductive ceramic Li_{6.4}Ga_{0.2}La₃Zr₂O₁₂ (LGLZO) in polyethylene oxide (PEO)/Li-bis (trifluoromethanesulfonyl) imide (LiTFSI) system. Compared to Li_{6.5}La₃Zr_{1.5}Ta_{0.5}O₁₂ (LLZTO), LGLZO provides better Li⁺ conductivity; therefore, a fast Li⁺ conducting pathway will form in the bulk of LGLZO

nanofillers. Besides, LGLZO nanofiller accelerates the dissociation of LiTFSI and benefits the transfer of free Li⁺ through the SPEs near the LGLZO surface, forming another interface fast Li⁺ conducting pathway in the SPEs. Benefits from the dual fast Li⁺ pathway design, the composite electrolyte membrane with 15 wt% LGLZO nanoparticles presents a high ionic conductivity of 8.0×10^{-4} S cm⁻¹ at 60 °C. The Li–Li symmetric cells with optimized content LGLZO show good cycling stability (no short circuit even after 1000 h), and the all-solid Li/LiFePO₄ batteries exhibit excellent cycling performance (remained 154 mAh g⁻¹ after 500 cycles at 0.2 C under 60 °C).

Introduction

Lithium-ion batteries (LIBs) offer a wide range of applications in energy storage due to their expansive voltage windows, high energy density, extended cycle life, and excellent charge/discharge efficiency. Traditional liquid lithium metal batteries (LMBs) have various safety issues, such as volatile organic liquid, flammability, and explosiveness, which make them unsuitable for large-scale commercial manufacture. These drawbacks of LMB can be overcome by using solid-state electrolytes (SSEs).^[1,2] SSEs can provide additional benefits, such as resistance to abrupt shocks and vibrations, in addition to the benefits of high safety, high energy density, cheap cost, and environmental friendliness. As a result, numerous automobile businesses have worked hard to produce all-solid-state lithium metal batteries (ASSLMB) that meet safety and efficiency standards.^[3–6]

Extensive investigation has been conducted on four types of solid-state electrolytes to broaden the potential application areas of ASSLMB. These electrolytes include solid polymer electrolytes (SPEs),^[7,8] inorganic ceramic oxides (ICEs),^[9,10] sulfide electrolytes (SEs),^[11,12] and halide electrolytes (HEs).^[13,14] SEs and

HEs are highly sensitive to air, while ICEs exhibit a higher interfacial impedance. SPE is a promising performer in ASSLMB due to its flexibility and simplicity of encapsulation, good elasticity, simple preparation method, and inexpensive cost compared to other electrolytes. PEO-based solid polymer electrolytes (SPEs) are widely used because of their good solubility of lithium salts and low glass transition temperatures.^[15–18] An ideal SPE should possess high Li⁺ conductivity, a high lithium-ion transfer number, and excellent thermal and electrochemical stability.^[19] However, the high crystallinity of PEO leads to a low Li⁺ conductivity of only $10^{-8} \sim 10^{-7}$ S cm⁻¹ and a low Li⁺ transference number at room temperature.

Inorganic fillers dispersed in PEO-based SPEs to construct composite polymer electrolytes (CSPEs) have been found to decrease PEO crystallinity and hence boost Li⁺ conductivity.^[20,21] Inorganic fillers are classified into two types: inert fillers that do not participate in Li⁺ transport (e.g., SiO₂, Al₂O₃, TiO₂) and active fillers that participate in Li⁺ transport.^[22–24] Activated ceramics (such as garnet-type Li₇La₃Zr₂O₁₂ (LLZO), stannic acid-type Li_{3.3}La_{0.56}TiO₃ (LLTO), NASICON conductors Li_xAl_xTi_{2-x}(PO₄)₃ (LATP), LISICON conductors, and Li₃N) in SPEs have the unique advantage of allowing Li⁺ to pass through the filler itself, especially when the Li⁺ conductors form percolation pathways.^[25–27] In addition to lowering the crystallinity of PEO-based polymers, the Lewis acid sites on the active filler's surface can dissociate lithium salts (LiTFSI), adsorb lithium salt anions (TFSI⁻) and release more free Li⁺ in the SPEs to improve the Li⁺ conductivity.^[28,29] Therefore, the active filler performs more effectively in improving Li⁺ conductivity and is held to higher expectations.

Garnet-type Li₇La₃Zr₂O₁₂ (LLZO) is highly valued for its outstanding features of high Li⁺ conductivity and stability

[a] Y. He, Dr. J. Tang, Dr. X. Huang, Prof. B. Tian

International Collaborative Laboratory of 2D Materials for Optoelectronics Science and Technology of Ministry of Education, Institute of Microscale Optoelectronics, Shenzhen University, Shenzhen 518060, China
E-mail: tianbb2011@szu.edu.cn

[b] Prof. X. Ao

Department of Materials Science and Engineering, School of Physics and Materials Science, Nanchang University, Nanchang 330031, China
E-mail: aoxin@ncu.edu.cn

 Supporting information for this article is available on the WWW under <https://doi.org/10.1002/batt.202400075>

toward lithium metals. Several metal elements, including Ta, Ga, and Al, have previously been used in investigations to stabilize the cubic phase of LLZO. Since the high Li^+ conducting property, LLZO is added into PEO-based solid electrolytes to improve electrolyte performance.^[30–32] However, in this literature, Ta-doped LLZO (LLZTO) is constantly utilized as a nano-filler in these publications, and the changes in Li^+ conductivity, among other elements of doped LLZO, are ignored. Among the LLZO family members with various doped elements, Ga-doped LLZO (LGLZO) has the highest Li^+ conductivity and excellent outcomes in increasing battery performance. It is attributed to gallium atoms' ability to produce Li vacancies in LLZO and promote the random distribution of Li on effective sites, considerably increasing ionic conductivity.^[33–40] Regrettably, the effect of Ga-doped LLZO on SPE performance has received little attention thus far.

In this work, we design a composite solid polymer electrolyte with bulk and interface dual fast Li^+ conducting pathway by incorporating LGLZO in polyethylene oxide (PEO)/Li-bis(trifluoromethanesulfonyl) imide (LiTFSI) system. Figure 1a illustrates the electrolyte membrane preparation procedure. Compared to the other elements doped LLZO (e.g., LLZTO), the LGLZO provides higher Li^+ conductivity; therefore, a fast Li^+ conducting pathway will be formed in the bulk of the LGLZO nanofillers. Additionally, the large Lewis acid-rich sites on the surface of LGLZO nanofillers accelerate the dissociation of LiTFSI, which makes it easier for the free Li^+ to pass through the SPE close to the surface of LGLZO and thus form another fast Li^+ transport pathway in the interfacial region located at the SPE (Figure 1b). Conversely, polymers near the LLZTO surface have limited availability of free Li^+ ions, resulting in a slower rate of Li^+ conduction. Thus, LGLZO is preferable to LLZTO in terms of enhancing the Li^+ conductivity of the CSPEs. CSPE-xLGLZO or CSPE-xLLZTO (where x% reflects the mass

content of LGLZO or LLZTO particles) are the CSPEs with different LGLZO or LLZTO particle contents. According to experimental results, the Li^+ conductivity of CSPE-15LGLZO electrolyte reaches $8.0 \times 10^{-4} \text{ Scm}^{-1}$ at 60°C , with a Li^+ transference number of 0.36, exceeding LLZTO-modified SPEs. Furthermore, various electrochemical and characterization tests are conducted to explore the internal mechanisms of the improvement. Benefiting from the favorable performance of CSPE with LGLZO, the ASSLMB assembled with LiFePO_4 as the positive electrode delivers an initial discharge capacity of 163 mAhg^{-1} at 60°C and 0.2 C and maintains a discharge capacity of 154 mAhg^{-1} with a Coulomb efficiency of 99% after 500 cycles of stabilization.

Results and Discussion

Various characterization and testing methods are used to investigate the physicochemical and electrochemical properties of CSPEs. X-ray diffraction (XRD) patterns (Figure 2a) of CSPE-15LLZTO and CSPE-15LGLZO exhibit the characteristic peaks of LLZTO and LGLZO. The results show that adding LLZTO or LGLZO weakens the crystalline peaks (120) and (112) of PEO, indicating a decrease in PEO crystallinity and an enhancement of PEO chain dipole moment.^[41,42] Based on the XRD data, the crystallinity of PEO in SPE-blank, CSPE-15LLZTO, and CSPE-15LGLZO is calculated to be 58.15%, 40.14%, and 33.17%, respectively (Figure S1, Supporting Information). DSC curves of these three SPEs (Figure 2b) are examined further to illustrate the phase transition characteristics of the electrolyte membranes. The addition of LGLZO to CSPE-15LGLZO leads to a lower glass transition temperature (T_g) (-51.5°C) compared to CSPE-15LLZTO (-49.5°C), and both are significantly lower than that of SPE-blank (-40.5°C), which further confirms that the

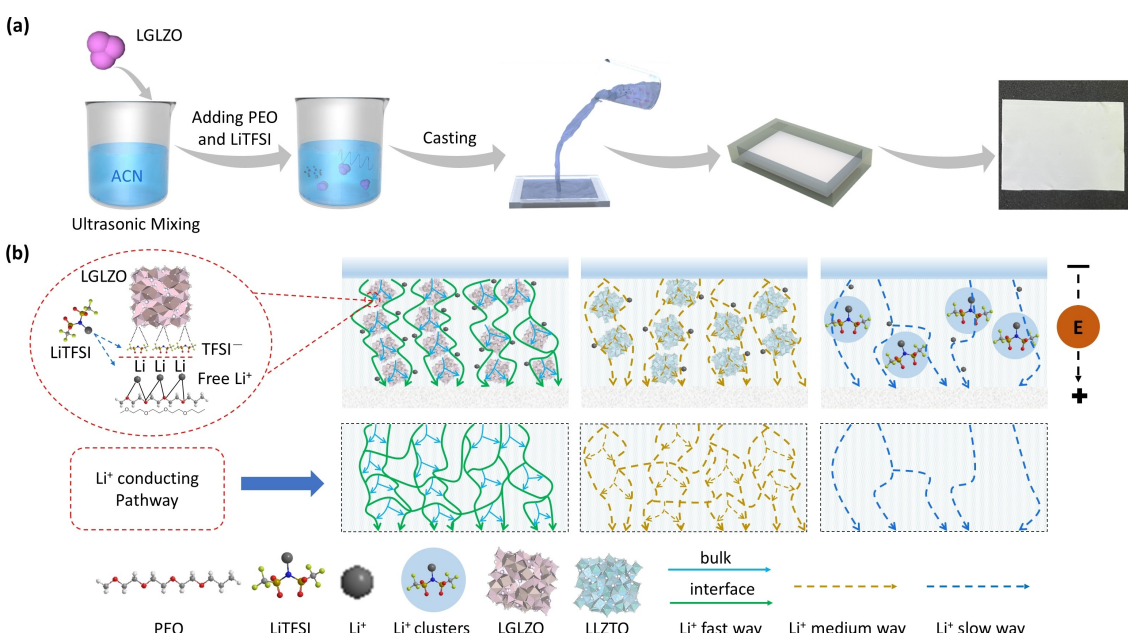


Figure 1. a) Schematic diagram of the synthesis process, and b) Li^+ conduction mechanism of the prepared CSPEs.

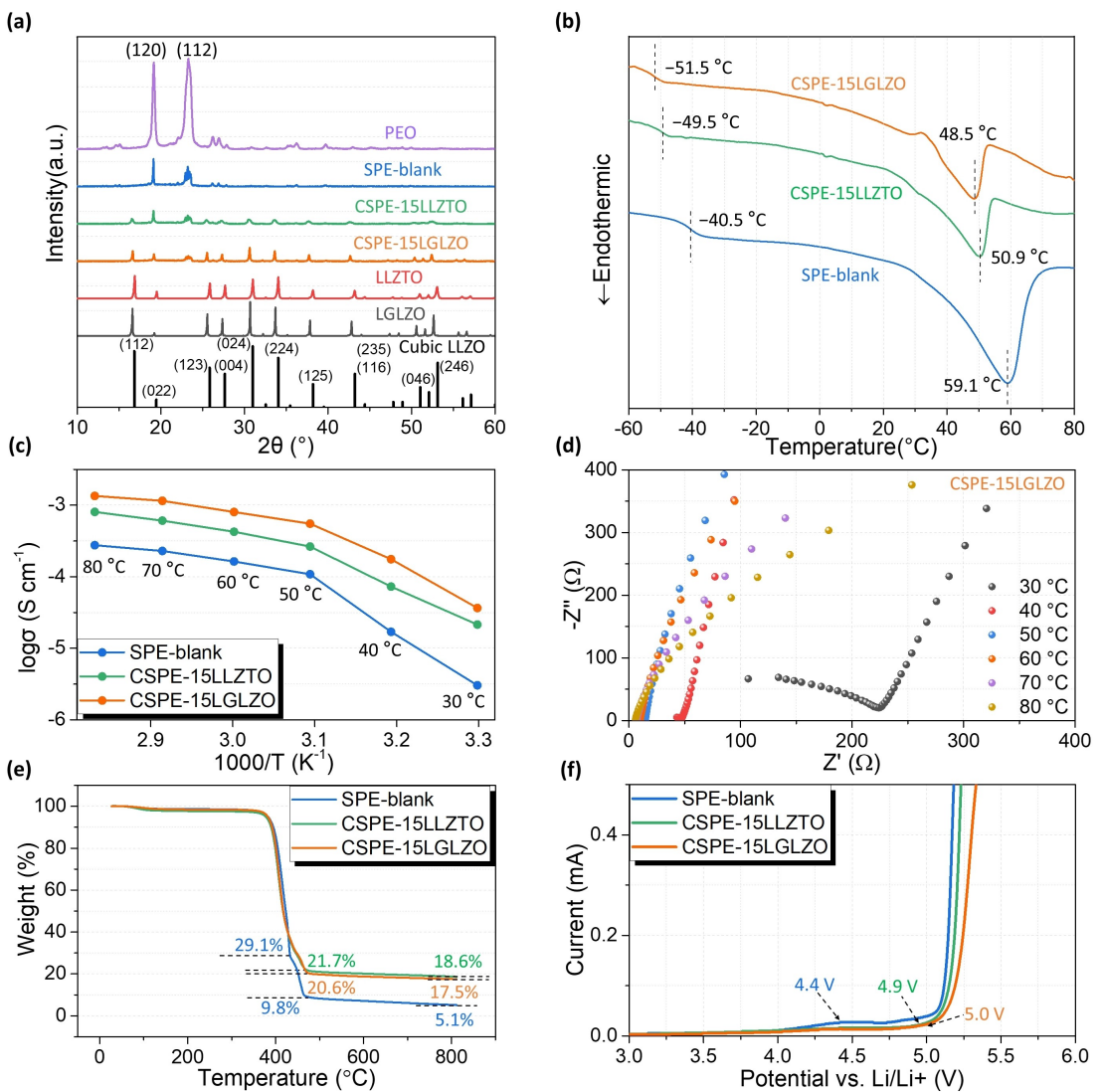


Figure 2. a) XRD spectra, b) DSC curves of SPE-blank, CSPE-15LLZTO, and CSPE-15LGLZO, c) Temperature dependence of the ionic conductivities of SPE-blank, CSPE-15LLZTO, and CSPE-15LGLZO, d) Impedance spectra of SS/(PEO/LiTFSI/15LGLZO)/SS cell from 30 to 80 °C, e) TGA curves, and f) LSV curves (sweep rate: 1 mVs⁻¹ at 60 °C) of SPE-blank, CSPE-15LLZTO, and CSPE-15LGLZO.

presence of LGLZO reduces the crystallinity of PEO. The temperature-dependent Li⁺ conductivity curves (Figure 2c) show that the Li⁺ conductivity reaches a maximum at 15 wt% LGLZO content, and the Li⁺ conductivity decreases with higher filler concentration (Figure S2, Supporting Information). This decrease is more likely attributed to the accumulation of LGLZO particles and reduced available free volume within the polymer.^[43] The electrochemical impedance spectra (EIS) curves of CSPE-15LGLZO, CSPE-15LLZTO and SPE-blank are observed at different temperatures (Figure 2d and Figure S3, Supporting Information). The Li⁺ conductivity of CSPE-15LGLZO is $8.0 \times 10^{-4} \text{ S cm}^{-1}$ at 60 °C. This value is significantly higher than that of CSPE-15LLZTO ($3.7 \times 10^{-4} \text{ S cm}^{-1}$) and SPE-blank ($1.6 \times 10^{-4} \text{ S cm}^{-1}$). The thermogravimetric analysis curves (TGA) (Figure 2e) are used to observe the thermal stability of the three electrolyte membranes. The weight loss of the three samples is approximately 2% to 3% until 300 °C, primarily due to water

absorption from the atmosphere. Between 350 and 680 °C, the weight loss mainly results from the decomposition of PEO and LiTFSI. Ultimately, the remaining masses of SPE-blank, CSPE-15LLZTO, and CSPE-15LGLZO are 5.1%, 18.6%, and 17.5%, respectively. The minor differences between the latter two groups are primarily attributed to the exceptional thermal stability of LGLZO and LLZTO. As a result, the differences with SPE-blank mainly stem from the superior thermal stability of LGLZO and LLZTO and, consequently, SPE. The Li/SPES/SS battery conducts a linear scan (LSV) at 60 °C to evaluate the electrochemical window (Figure 2f). CSPE-15LGLZO exhibits a stable plateau surpassing that of CSPE-15LLZTO (~4.9 V) and SPE-blank (~4.4 V), demonstrating an elevated plateau around 5.0 V. The increased electrochemical stability of CSPE-15LGLZO can be attributed to the excellent chemical stability of LGLZO, which contributes 15 wt%. This addition effectively diminishes direct contact at the interface between lithium metal and PEO,

reduces the occurrence of adverse side effects, and broadens PEO's electrochemical chemistry window. Additionally, the tensile stress-strain curves for the three electrolytes (Figure S4, Supporting Information) and the stress-strain curve data (Table S1, Supporting Information) reveal that CSPE-15LGLZO exhibits a maximum stress of 1.0 MPa, higher than both CSPE-15LLZTO (0.93 MPa) and SPE-blank (0.66 MPa). The results indicate that the adding LGLZO particles to SPEs enhances the toughness and strength of CSPEs.

⁷Li NMR results (Figure S5, Supporting Information) show that the half-peak width of LGLZO is narrower compared with that of LLZTO, which indicates that Li⁺ ions migrate faster inside LGLZO than inside LLZTO, which is favorable for the formation of richer Lewis acid sites on the LGLZO surface. Adding LGLZO can expand the amorphous region of SPEs, and the numerous Lewis acid sites on the surface of LGLZO can limit TFSI⁻ ion migration and generate a fast Li⁺ conduction path in SPEs. At the same time, the interior of LGLZO can rapidly move Li⁺, allowing additional free Li⁺ to be accessible for migration. Figure 3a and Figure S6 (Supporting Information) display the complete FTIR spectra of SPE-blank, CSPE-15LLZTO, and CSPE-15LGLZO within the 1400 to 1150 cm⁻¹ range, as well as the detailed FTIR spectra within the 4000 to 400 cm⁻¹ range. By combining the FTIR spectra of PEO and LiTFSI (Figure S7, Supporting Information), we can observe the main peaks of PEO around 1358, 1342, 1279, and 1241 cm⁻¹. The main peaks corresponding to the asymmetric and symmetric stretching of

-SO₂ and -CF₃ in LiTFSI are found. When LiTFSI is dissolved into the PEO matrix, peak shifts, and splitting are observed near 1325, 1245, and 1199 cm⁻¹, signifying the dissociation of LiTFSI in the PEO polymer. Subsequently, the addition of 15LGLZO filler to the PEO/LiTFSI system results in peak shifts at 1333.32 and 1299.77 cm⁻¹ corresponding to -SO₂ stretching, which shifts to 1335.53 and 1294.38 cm⁻¹, respectively. Similarly, for the symmetric stretching of -CF₃, the peaks move from 1252.87 and 1228.82 cm⁻¹ to 1252.07 and 1229.84 cm⁻¹, and for the asymmetric extension of -CF₃, similar peak shifts are observed from 1201.90 and 1185.23 cm⁻¹ to 1199.64 and 1184.39 cm⁻¹, respectively. The shifts of the corresponding peaks due to these structural stretches in CSPE-15LGLZO are greater than those in CSPE-15LLZTO.^[42,44-46] The state of LiTFSI in the electrolyte can be studied by analyzing the Raman spectra, which are highly sensitive to the changes of LiTFSI in SPE. This sensitivity is observed in the wavelength range from 720 to 760 cm⁻¹, corresponding to the vibration of TFSI only. In the Raman spectra of SPE-blank, CSPE-15LLZTO, and CSPE-15LGLZO (Figure 3b), two Lorentz peaks near 740 cm⁻¹ (L1) and 745 cm⁻¹ (L2) can be identified. L1 corresponds to free TFSI⁻, while L2 corresponds to ion cluster LiTFSI.^[41,44,47] By fitting and semi-quantitatively estimating the relative values of ion association and solvation of LiTFSI in different electrolytes, the percentage of "free TFSI⁻" and "ion cluster" can be calculated. This calculation similarly considers the scattering cross sections of

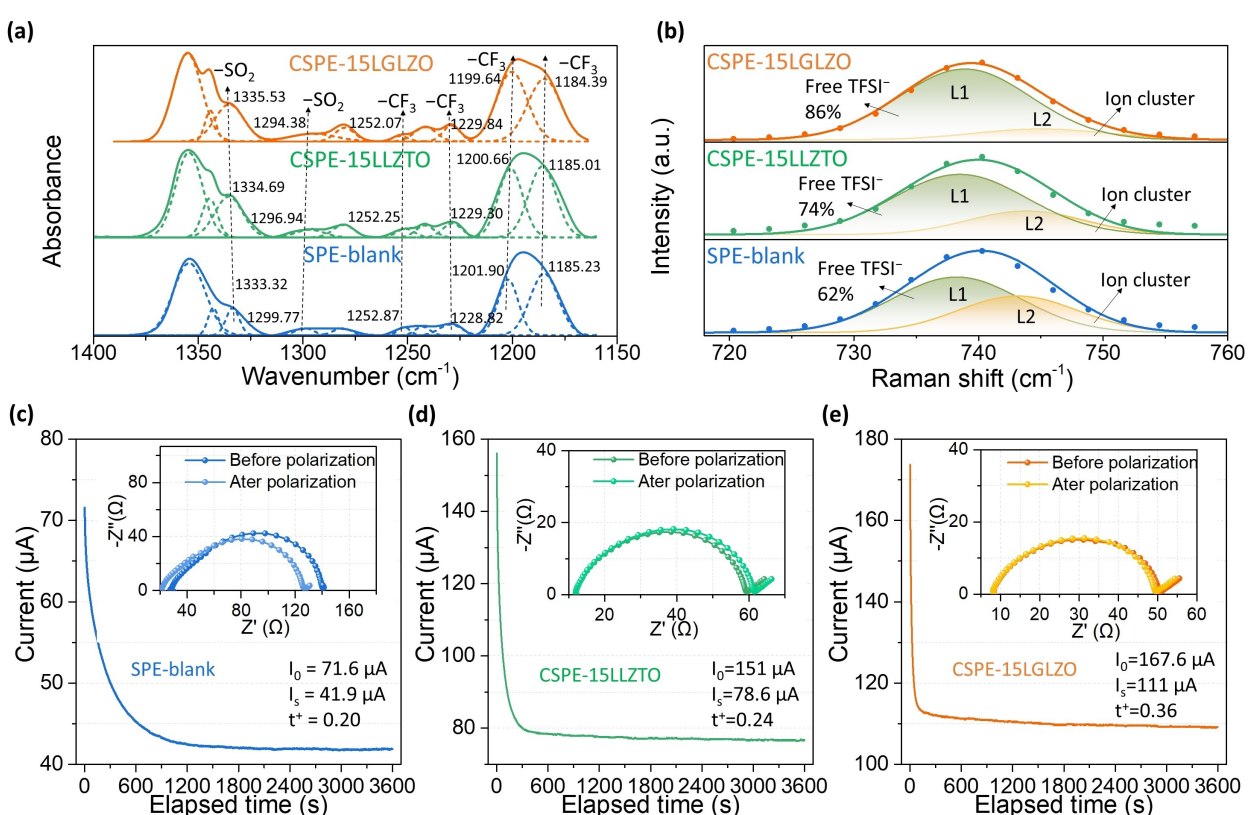


Figure 3. a) FTIR spectra of SPE-blank, CSPE-15LLZTO and CSPE-15LGLZO at 1400~1150 cm⁻¹, b) Raman spectra of SPE-blank, CSPE-15LLZTO and CSPE-15LGLZO, the chronoamperometry (CA) curves of symmetric Li/Li batteries with an applied potential of 0.01 V at 60 °C and the EIS plots before and after polarization (inset) with c) SPE-blank, d) CSPE-15LLZTO, and e) CSPE-15LGLZO.

free TFSI⁻ and ion clusters. The equation used for calculating the percentage of "free TFSI⁻" is as follows:

$$\text{Free TFSI}^- = \frac{A_{L1}}{A_{L1} + A_{L2}} \times 100\% \quad (1)$$

where A(L1) is the integrated intensity of the L1 band and A(L2) is the integrated density of the L2 band.^[48–52] In SPE-blank, the percentage of free TFSI⁻ is 62%, suggesting the presence of numerous ion clusters. However, in CSPE-15LLZTO, the percentage of free TFSI⁻ is 74%, suggesting that many ionophores are still present. Conversely, in CSPE-15LGLZO, the L2 band is significantly reduced, and the percentage of free TFSI⁻ reached 86%, implying a better dissociation of ion clusters. Furthermore, the Li⁺ transference number (t^+) of CSPE-15LGLZO at 60 °C is 0.36, higher than that of CSPE-15LLZTO (0.24) and SPE-blank (0.20) (Figure 3c–e). This indicates stronger interactions between LGLZO particles and TFSI⁻ groups and an increased concentration of free Li⁺.

Critical current density (CCD) is an essential indicator to evaluate the resistance level of SPEs to Li dendrite penetration at high current densities in Li|SPE|Li symmetric cells (Figure 4a–c).^[44,53] The recent density increases at 0.05 mA cm⁻² (0.5 h stripping and 0.5 h plating) starting from 0.05 mA cm⁻². The CCD of CSPE-15LGLZO (0.65 mA cm⁻²) is higher than that of CSPE-15LLZTO (0.45 mA cm⁻²) and SPE-blank (0.1 mA cm⁻²). Analyzing the CCD helps understand the stability of the Li/electrolyte interface and the growth of Li dendrites. Li/SPE-blank/Li cells fail to charge and discharge correctly at 0.1 mA cm⁻² due to the generation of dendrites caused by the tendency of the interface to generate space charge fields even

at low current densities. In contrast, the Li/CSPE-15LGLZO interface is characterized by a fast Li⁺ channel, which enables the rapid transfer of Li⁺ without causing severe polarization. This unique feature of the Li/CSPE-15LGLZO interface results in a strong resistance against the formation of Li dendrites. As a result, the Li/CSPE-15LGLZO/Li cell exhibits a low polarization voltage and achieves a high CCD value even at high current densities. Figure 4d shows the stability test of the Li/CSPE-15LGLZO/Li cell, which involves 1000 h of constant-current cycling at a current density of 0.1 mA cm⁻² and a temperature of 60 °C. The initial EIS plots indicate that CSPE-15LGLZO most significantly lowers the interfacial resistance of the Li/Li cell as shown in Figure S8 (Supporting Information). The voltage plateau of the Li/CSPE-15LGLZO/Li cell remains flat and stable throughout the cycling, indicating that the cell exhibits low polarization voltage. In contrast, the polarization voltages of the Li/SPE-blank/Li and Li/CSPE-15LLZTO/Li cells increase continuously with cycles. After approximately 200 and 500 h, the polarization voltages of the Li/SPE-blank/Li and Li/CSPE-15LLZTO/Li cells drop to 0 V, respectively. This suggests that CSPE-15LGLZO possesses fast ion transport capability and high mechanical strength, which effectively inhibits the growth of Li dendrites and promotes the uniform deposition of Li during cycling.

The rate and polarization capabilities of Li/LiFePO₄ solid-state batteries are analyzed using cyclic voltammetry (CV) at 60 °C (Figure 5a and Figure S9, Supporting Information). The CV curves of the Li/CSPE-15LGLZO/LiFePO₄ cell show an oxidation peak at around 3.53 V and a reduction peak around 3.33 V when the sweep rate is set at 0.04 mV s⁻¹. These peaks are indicative of the debonding and embedding processes of

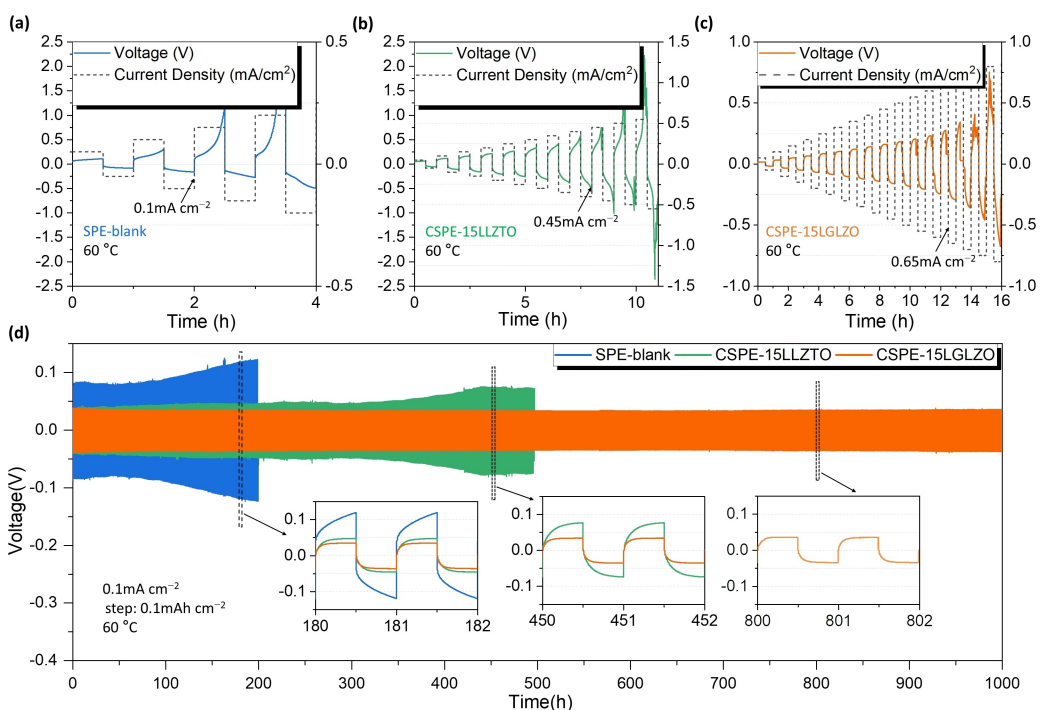


Figure 4. CCD curves a–c) of Li/SPE-blank/Li, Li/CSPE-15LLZTO/Li, and Li/CSPE-15LGLZO/Li at 60 °C, and d) Voltage–time curves of Li/SPE-blank/Li, Li/CSPE-15LLZTO/Li, and Li/CSPE-15LGLZO/Li at 60 °C, 0.1 mA cm⁻², and (inset) enlarged plot of the local voltage distribution.

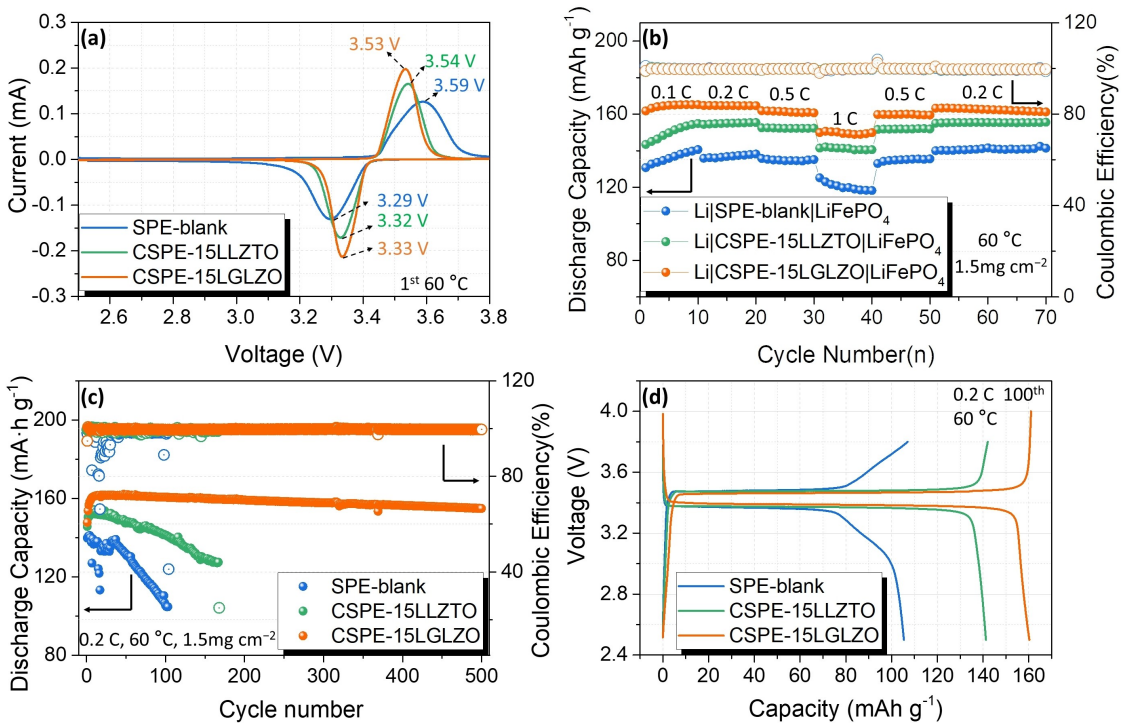


Figure 5. a) First cycle comparison of cyclic voltammetry (CV) curves for Li/SPE-blank/LiFePO₄, Li/CSPE-15LLZTO/LiFePO₄ and Li/CSPE-15LGLZO/LiFePO₄ at 60 °C with a sweep rate of 0.04 mV s⁻¹, b) rate performance of Li/LiFePO₄ battery at 60 °C, c) cycling performance of Li/LiFePO₄ battery at 60 °C and 0.2 C, and d) comparison of charge/discharge curves of Li/LiFePO₄ battery at 60 °C and 0.2 C for the 100th cycle.

Li⁺^[49,53–56] Compared to the Li/SPE-blank/LiFePO₄ and Li/CSPE-15LLZTO/LiFePO₄ cells, the Li/CSPE-15LGLZO/LiFePO₄ exhibits smaller voltage difference between the oxidation and reduction peaks, as well as higher peak oxidation and reduction currents. These results suggest that the Li/CSPE-15LGLZO/LiFePO₄ cell possesses greater electrochemical reversibility and fast electrochemical kinetics. Consequently, the CSPE-15LGLZO electrolyte offers improved constant current characteristics for solid-state lithium metal cells at 60 °C. Furthermore, the total resistance of the Li/CSPE-15LGLZO/LiFePO₄ cell is 43 Ω, lower than the total resistance of the Li/CSPE-15LLZTO/LiFePO₄ cell (55 Ω) and the Li/SPE-blank/LiFePO₄ cell (175 Ω), providing additional evidence for the effectiveness of the LGLZO filler (Figure S10, Supporting Information). The rate performance of Li/LiFePO₄ cells assembled with SPE-blank, CSPE-15LLZTO, and CSPE-15LGLZO is evaluated, as illustrated in Figure 5b. The Li/CSPE-15LGLZO/LiFePO₄ cell demonstrates discharge capacities of 165, 164, 161, and 150 mAh g⁻¹ at 0.1, 0.2, 0.5, and 1 C, respectively. In contrast, the maximum discharge capacities of Li/CSPE-15LGLZO/LiFePO₄ cell and Li/SPE-blank/LiFePO₄ cell at 0.1, 0.2, 0.5, and 1 C are merely 154, 154, 152, 142 mAh g⁻¹ and 140, 138, 135, 125 mAh g⁻¹, respectively. This observation suggests that incorporating LGLZO can substantially enhance the rate performance. The corresponding charge-discharge curves further corroborate the stability of the charge-discharge process across all rates, as depicted in Figure S11a (Supporting Information). The Li/LiFePO₄ battery incorporating CSPE-15LGLZO demonstrates commendable long-term cycling stability, maintaining a discharge capacity of 154 mAh g⁻¹ after

500 cycles at 0.2 C (Figure 5c). Conversely, the discharge capacity of the Li/LiFePO₄ battery with CSPE-15LLZTO and SPE-blank decrease to 127 mAh g⁻¹ after 165 cycles and 104 mAh g⁻¹ after 100 cycles at 0.2 C, respectively. Moreover, the Li/CSPE-15LGLZO/LiFePO₄ cell displays a more stable working platform and reduced polarization in comparison to the Li/CSPE-15LLZTO/LiFePO₄ cell and the Li/SPE-blank/LiFePO₄ cell (Figure 5d). This can be ascribed to the enhanced Li⁺ conductivity of CSPE following the integration of LGLZO particles into PEO-based SPEs, resulting in diminished resistance during the charge-discharge process. The Li/CSPE-15LGLZO/LiFePO₄ battery's charging and discharging curves at 0.2 C, with varying cycle turns, also confirm its outstanding cycle stability (Figure S11b, Supporting Information). The Li/LiFePO₄ cell with CSPE-15LGLZO maintains a discharge capacity of 154 mAh g⁻¹ after 150 cycles at 0.5 C and 139 mAh g⁻¹ after 500 cycles at 1 C under high-multiplier long cycling (Figure S12a–b, Supporting Information). The Li/LiFePO₄ cell employing CSPE-15LGLZO exhibits robust cycling stability even at 30 °C (Figure S12c–d, Supporting Information), with a specific capacity of 156 mAh g⁻¹ after 100 cycles at 0.1 C. In stark contrast, the Li/LiFePO₄ cell using SPE-blank performs inadequately at 30 °C. Furthermore, the Li/CSPE-15LGLZO/LiFePO₄ cell exhibits the ability to undergo 40 continuous cycles while maintaining a cathode active material loading of up to 4 mg cm⁻², achieving a specific capacity of up to 153.7 mAh g⁻¹. This exceptional performance is reinforced by the charging/discharging curves for different number of turns, providing a clear demonstration of its cycling stability (Figure S13a–b, Supporting Information). The advanta-

geous characteristics of CSPE-15LGLZO ensure that the all-solid-state lithium batteries exhibit superior capacity and capacity retention, extended cycle life, and enhanced stability.

Conclusions

In conclusion, the construction of dual fast Li⁺ conducting pathways, both on the bulk and interface level, endows a composite polymer solid-state electrolyte with active ceramic LGLZO particles with favorable Li⁺ conductivity. The abundant Li vacancies residing within the LGLZO facilitate a random Li distribution on effective sites, thus creating a rapid Li⁺ transport pathway within the bulk LGLZO. Moreover, the surface-rich Lewis acid sites on LGLZO particles assist in the dissociation of LiTFSI, instigating the formation of an additional fast Li⁺ transport pathway within the polymer matrix adjacent to the LGLZO particles. As a result of the aforementioned design, the PEO/LiTFSI-based composite electrolyte, containing 15 wt% content, exhibits exemplary Li⁺ conductivity (8.0×10^{-4} S cm⁻¹ at 60°C) and a high Li⁺ transfer number (0.36 at 60°C). The Li/CSPE-15LGLZO/Li cell showcases superior cycling stability at a current density of 0.1 mA cm⁻², demonstrating endurance over 1000 h without any occurrence of a short circuit. Furthermore, the all-solid-state Li/LiFePO₄ battery incorporating CSPE-15LGLZO demonstrates a high discharge capacity and outstanding cycling stability (154 mAh g⁻¹ at 0.2 C after 500 cycles while maintaining a Coulombic efficiency over 99%). This study presents a novel approach for establishing a dual fast Li⁺ conducting pathway in SPEs, capitalizing on the benefits of enhanced electrochemical performance, simplified fabrication process, and cost-effectiveness. These findings offer a propitious avenue for research into solid-state polymer electrolytes that prioritize safety and high performance.

Experimental Section

Materials: PEO (Aladdin, M_v=600,000 g mol⁻¹) and LiTFSI (Aladdin, 99%) were dried under vacuum at 65°C and 110°C, respectively, for more than 24 h. After drying, the above materials were placed in a glove box filled with argon gas (less than 0.01 ppm H₂O and O₂).

Preparation of Ga-LLZO Particles: In this work, Ga-doped (Ga=0.2) LLZO particles were added into the SPEs. LGLZO particles with Ga=0.2 doping level is confirmed as having the highest Li⁺ conductivity (Figure S14, Supporting Information), which is consistent with our previous work.^[57–61]

A conventional solid-phase synthesis method prepared LGLZO with the nominal composition of Li_{6.4}Ga_{0.2}La₂Zr₂O₁₂, in the stoichiometric ratios of LiOH·H₂O (AR, 98%), La₂O₃ (99.99%, preheated at 900°C for 12 h), ZrO₂ (AR, 3 N), and Ga₂O₃ (AR, 99.99%) of the starting materials (total 0.2 mol, ~169 g) were weighed, and the Li source has not overdosed. Then isopropyl alcohol (IPA, 300–350 g) was used as a solvent, and yttria-stabilized zirconia (YSZ) beads (Φ 10 mm, 100 g; Φ 5 mm, 600 g) as grinding media, were ball milled in a ball mill (MITR) at 200 rpm for 12 h. After drying at 65°C, 80 g of the precursor powder was taken and calcined in a MgO crucible without a lid at 850°C for 6 h to obtain the cubic phase powder.

The powder was then wet ball-milled again at 120 rpm for 6 h, dried and sieved through 200 mesh to obtain Ga-LLZO powder with particle size close to the nanoscale, dried under vacuum at 60°C and taken into a glove box for further use (Figure S15, Supporting Information). Li_{6.5}La₃Zr_{1.5}Ta_{0.5}O₁₂ (0.2 mol, ~176 g) was also prepared as shown above using Ta₂O₅ (AR, 99.5%), with the difference that 80 g of the precursor powder was taken and calcined at 950°C for 6 h without cover to obtain the cubic phase powder with a 10% excess of Li source (Figure S16, Supporting Information).

Preparation of Composite Solid Electrolytes: The composite SPEs were prepared by solution casting method in a glove box. As an example, the SPEs modified with LGLZO particles were first, LGLZO powders with different mass fractions (0 wt%, 5 wt%, 10 wt%, 15 wt%, 20 wt%) were added to 10 mL of acetonitrile (1 g PEO~20 mL CH₃CN) and ultrasonically mixed for 10 min, and then 0.5524 g of PEO and 0.2 g of LiTFSI dissolved in acetonitrile were stirred together with the LGLZO for 12 h to obtain a uniform mixture (EO:Li=18:1). The viscous solution was poured into a Teflon mould and dried in a glove box for 12 h, followed by further drying in a vacuum oven at 60°C for 12 h to remove the residual acetonitrile solution. CSPE-15LLZTO was prepared as described above for the preparation process.

Material Characteristics: The morphological structures of the prepared LGLZO and LLZTO particles and the morphology of the electrolyte membrane surfaces and sections were observed by field emission scanning electron microscopy (SEM, TESCAN-MIRA3). Elemental mapping was performed on energy-dispersive X-ray spectroscopy (EDS). The physical phases of the powders and electrolyte membranes were determined by X-ray diffraction (XRD) (Rigaku Ultima IV, nickel-filtered Cu K α radiation, $\lambda=1.542$ Å) at a scan rate of 6° min⁻¹ over a 20 range from 10° to 60°. T_g and T_m of the three membranes were obtained by differential scanning calorimetry (DSC, NETZSCH, low-temperature DSC-200 F3) at a heating rate of 10°C min⁻¹ in the range of -100°C to 100°C. The tests were performed on a TG analyzer (NETZSCH STA 449F5) at a heating rate of 5°C min⁻¹ over the temperature range of room temperature to 1000°C in air. Spectra between 400 and 4000 cm⁻¹ were measured by FTIR spectroscopy (Bruker VERTEX 70 V). Raman spectra were obtained at room temperature using a Raman spectrometer (WITec alpha300R, laser wavelength of 532 nm). The stress-strain curves of the three prepared SPEs were tested by an electronic universal testing machine (INSTRON 3343).

Electrochemical Testing: All coin cells were assembled in a glove box and stored in a constant temperature chamber awaiting testing. Electrochemical impedance spectroscopy (EIS) tests were performed using an AC impedance spectrometer (IVIUM nSTAT) with a frequency range of 0.1 Hz to 1 MHz and a bias voltage of 10 mV. Coin cell cases of type CR2016 were used for assembly, and the electrolyte membrane (thickness ~150 μm) was sandwiched between two stainless steel plates (diameter = 16 mm) and tested at a temperature range of 30°C to 80°C. The AC impedance spectra (EIS) of the electrolyte membranes at different temperatures were obtained by this method to calculate the Li⁺ conductivity of the corresponding electrolytes.

The calculation equation is as follows:

$$\sigma = \frac{L}{RS} \quad (2)$$

where σ is the Li⁺ conductivity, L is the thickness of the electrolyte membrane, R is the intrinsic impedance of the electrolyte (intercept

of the Nyquist plot on the x-axis), and S is the effective area of the electrolyte.

Assembled with two lithium metal cells (diameter = 16 mm) as non-blocking electrodes using CR2032-type coin cell cases. The Li⁺ mobility of the electrolyte membrane was measured by the chrono-current method (potential applied to the cell was 10 mV) and AC impedance spectroscopy, calculated as follows:

$$t^+ = \frac{I_{ss}(\Delta V - I_0 R_0)}{I_0(\Delta V - I_{ss} R_{ss})} \quad (3)$$

where t⁺ is the Li⁺ transfer number, I₀ and I_{ss} represent the initial and steady-state currents, respectively, ΔV denotes the external polarization voltage (10 mV), and R₀ and R_{ss} represent the electrolyte/Li interface resistance in the initial and steady states.

The electrochemical stability of the stainless steel (SS)/SPEs/Li sheet (Li) cell from 0 to 6 V vs Li/Li⁺ at 1 mV s⁻¹ was tested by linear scanning voltammetry using a CR2016-type coin cell case. For the cell performance test using LiFePO₄ cathode, LiFePO₄, super P and polyvinylidene fluoride S6 (PVDF) were mixed in NMP in the mass ratio of 7:2:1. After mixing well, the slurry was cast on aluminium foil for squeegee coating and dried under vacuum at 60°C for 12 h. The loadings of active materials for the cathode in the experiments were about 1.5 and 4.0 mg cm⁻², and the thickness of the electrolyte membrane was about 100 μm (Figure S17, Supporting Information). The CR2016-type coin cell shell was used, and lithium metal was used as the anode for the assembly. Constant current charging and discharging tests (1 C = 170 mAh g⁻¹) were performed at 30°C and 60°C by the Neware test system (Shenzhen Neware Technology Limited). All cells were tested between 2.5 V and 3.8 V at 30°C and 60°C, except for the Li/CSPE-15LGLZO/LiFePO₄ cell at 0.2 C, which was tested between 2.5 V and 4.0 V to investigate its cycling stability when charged and discharged to higher potentials.

Supporting Information

Supporting Information is available from the Wiley Online Library or from the author.

Acknowledgements

The authors gratefully acknowledge the financial support from the Science and Technology Project of Shenzhen (Grant Nos. JCYJ20210324094206019 and JCYJ20210324094000001), the National Natural Science Foundation of China (52262036) and the Guangdong Mache Power Technology Co., Ltd.

Conflict of Interests

The authors declare no conflict of interest.

Data Availability Statement

The data that support the findings of this study are available from the corresponding author upon reasonable request.

Keywords: all-solid Li/LiFePO₄ batteries · composite electrolyte membrane · dual fast Li⁺ conducting pathway · Li_{6.4}Ga_{0.2}La₃Zr₂O₁₂ · solid polymer electrolytes

- [1] M. Armand, J. M. Tarascon, *Nature* **2008**, *451*(7179), 652.
- [2] D. P. Lu, Y. Y. Shao, T. Lozano, W. D. Bennett, G. L. Graff, B. Polzin, J. G. Zhang, M. H. Engelhard, N. T. Saenz, W. A. Henderson, P. Bhattacharya, J. Liu, J. Xiao, *Adv. Energy Mater.* **2015**, *5* (3), 7.
- [3] S. Abada, G. Marlair, A. Lecocq, M. Petit, V. Sauvant-Moynot, F. Huet, *J. Power Sources* **2016**, *306*, 178.
- [4] J. C. Bachman, S. Muy, A. Grimaud, H. H. Chang, N. Pour, S. F. Lux, O. Paschos, F. Maglia, S. Lupart, P. Lamp, L. Giordano, Y. Shao-Horn, *Chem. Rev.* **2016**, *116*(1), 140.
- [5] F. Zheng, M. Kotobuki, S. F. Song, M. O. Lai, L. Lu, *J. Power Sources* **2018**, *389*, 198.
- [6] J. Zhu, T. Wierzbicki, W. Li, *J. Power Sources* **2018**, *378*, 153.
- [7] Z. G. Xue, D. He, X. L. Xie, *J. Mater. Chem. A* **2015**, *3*(38), 19218.
- [8] K. Faliya, H. Klem, *Electrochim. Acta* **2018**, *290*, 211.
- [9] V. Thangadurai, W. Weppner, *Adv. Funct. Mater.* **2005**, *15*(1), 107.
- [10] E. J. Cussen, *Chem. Commun.* **2006**, *4*, 412.
- [11] J. Lau, R. H. DeBlock, D. M. Butts, D. S. Ashby, C. S. Choi, B. S. Dunn, *Adv. Energy Mater.* **2018**, *8*(27), 1800933.
- [12] J. H. Wu, S. F. Liu, F. D. Han, X. Y. Yao, C. S. Wang, *Adv. Mater.* **2021**, *33*(6), 2000751.
- [13] M. Dondelinger, J. Swanson, G. Nasymov, C. Jahnke, Q. Q. Qiao, J. Wu, C. Widener, A. Numan-Al-Mobin, A. Smirnova, *Electrochim. Acta* **2019**, *306*, 498.
- [14] C. Rosenbach, F. Walther, J. Ruhl, M. Hartmann, T. A. Hendriks, S. Ohno, J. Janek, W. Zeier, *Adv. Energy Mater.* **2023**, *13*(6), 2203673.
- [15] N. C. Rosero-Navarro, R. Kajiura, R. Jalem, Y. Tateyama, A. Miura, K. Tadanaga, *ACS Appl. Energ. Mater.* **2020**, *3*(6), 5533.
- [16] L. Chen, X. M. Qiu, Z. M. Bai, L. Z. Fan, *J. Energy Chem.* **2021**, *52*, 210.
- [17] A. Baniya, A. Gurung, J. Pokharel, K. Chen, R. Pathak, B. S. Lamsal, N. Ghimire, R. S. Bobba, S. I. Rahman, S. Mabrouk, A. L. Smirnova, K. Xu, Q. Qiao, *ACS Appl. Energ. Mater.* **2022**, *5*(1), 648.
- [18] J. P. Vivek, N. Meddings, N. Garcia-Araez, *ACS Appl. Mater. Interfaces* **2022**, *14*(1), 633.
- [19] D. Zhou, D. Shanmukaraj, A. Tkacheva, M. Armand, C. X. Wang, *Chem* **2019**, *5*(9), 2326.
- [20] A. Arya, A. L. Sharma, *Ionics* **2017**, *23*(3), 497.
- [21] S. J. Tan, X. X. Zeng, Q. Ma, X. W. Wu, Y. G. Guo, *Electrochim. Energy. R* **2018**, *1*(2), 113.
- [22] L. Z. Fan, C. W. Nan, S. J. Zhao, *Solid State Ionics* **2003**, *164*(1–2), 81.
- [23] C. C. Tambelli, A. C. Bloise, A. Rosario, E. C. Pereira, C. J. Magon, J. P. Donoso, *Electrochim. Acta* **2002**, *47*(11), 1677.
- [24] P. K. Singh, B. Bhattacharya, R. K. Nagarale, *J. Appl. Polym. Sci.* **2010**, *118*(5), 2976.
- [25] Z. Wang, L. Gao, Y. S. Ding, B. Wu, H. J. Zhou, P. He, S. M. Dong, *Ceram. Int.* **2012**, *38*(1), 535.
- [26] M. Dirican, C. Y. Yan, P. Zhu, X. W. Zhang, *Mat. Sci. Eng. R* **2019**, *136*, 27.
- [27] L. C. Wang, Z. S. Chen, Y. H. Zhang, C. Liu, J. P. Yuan, Y. L. Liu, W. Y. Ge, S. Lin, Q. An, Z. G. Feng, *Chem. Asian J.* **2022**, *17*(15), e202200278.
- [28] X. Shen, R. Y. Li, H. S. Ma, L. Q. Peng, B. Y. Huang, P. Zhang, J. B. Zhao, *Solid State Ionics* **2020**, *354*, 115412.
- [29] A. K. Chauhan, K. Mishra, D. Kumar, A. Singh, *J. Electron. Mater.* **2021**, *50*(9), 5122.
- [30] W. F. Wei, L. Li, L. Zhang, J. H. Hong, G. He, *Electrochim. Commun.* **2018**, *90*, 21.
- [31] Z. Y. Huang, W. Y. Pang, P. Liang, Z. H. Jin, N. Grundish, Y. T. Li, C. A. Wang, *J. Mater. Chem. A* **2019**, *7*(27), 16425.
- [32] J. Cheng, G. M. Hou, Q. Sun, Q. Chen, D. P. Li, J. W. Li, Z. Zeng, K. K. Li, Q. H. Yuan, J. J. Wang, L. J. Ci, *Sci. China Mater.* **2022**, *65*(2), 364.
- [33] G. Han, B. Kinzer, R. Garcia-Mendez, H. Choe, J. Wolfenstine, J. Sakamoto, *J. Eur. Ceram. Soc.* **2020**, *40*(54), 1999.
- [34] M. Philipp, B. Gadermaier, P. Posch, I. Hanzu, S. Ganschow, M. Meven, D. Rettenwander, G. J. Redhammer, H. M. R. Wilkening, *Adv. Mater. Interfaces* **2020**, *7*(16), 2000450.
- [35] C. Y. Huang, Y. T. Tseng, H. Y. Lo, J. K. Chang, W. W. Wu, *Nano Energy* **2020**, *71*, 104625.
- [36] Z. Li, H. X. Xie, X. Y. Zhang, X. Guo, *J. Mater. Chem. A* **2020**, *8*(7), 3892.
- [37] X. Y. Tao, L. Yang, J. L. Liu, Z. H. Zang, P. Zeng, C. F. Zou, L. G. Yi, X. Y. Chen, L. Liu, X. Y. Wang, *J. Alloys Compd.* **2023**, *937*, 168380.

- [38] X. Huang, J. M. Su, Z. Song, T. P. Xiu, J. Jin, M. E. Badding, Z. Y. Wen, *Ceram. Int.* **2021**, *47*(2), 2123.
- [39] P. Badami, J. M. Weller, A. Wahab, G. Redhammer, L. Ladenstein, D. Rettenwander, M. Wilkening, C. K. Chan, A. N. M. Kannan, *ACS Appl. Mater. Interfaces* **2020**, *12*(43), 48580.
- [40] M. Y. Yi, T. Liu, X. N. Wang, J. Y. Li, C. Wang, Y. C. Mo, *Ceram. Int.* **2019**, *45*(1), 786.
- [41] X. Ao, X. T. Wang, J. W. Tan, S. L. Zhang, C. L. Su, L. Dong, M. X. Tang, Z. C. Wang, B. B. Tian, H. H. Wang, *Nano Energy* **2021**, *79*, 105475.
- [42] H. Chen, D. Adekoya, L. Hencz, J. Ma, S. Chen, C. Yan, H. J. Zhao, G. L. Cui, S. Q. Zhang, *Adv. Energy Mater.* **2020**, *10*(21), 2000049.
- [43] S. Suriyakumar, S. Gopi, M. Kathiresan, S. Bose, E. B. Gowd, J. R. Nair, N. Angulakshmi, G. Meligrana, F. Bella, C. Gerbaldi, A. M. Stephan, *Electrochim. Acta* **2018**, *285*, 355.
- [44] J. B. Kang, Z. R. Yan, L. Gao, Y. F. Zhang, W. C. Liu, Q. Yang, Y. X. Zhao, N. P. Deng, P. B. W. Cheng, W. M. Kang, *Energy Storage Mater.* **2022**, *53*, 192.
- [45] Y. Lin, X. M. Wang, J. Liu, J. D. Miller, *Nano Energy* **2017**, *31*, 478.
- [46] S. J. Wen, T. J. Richardson, D. I. Ghantous, K. A. Streibel, P. N. Ross, E. J. Cairns, *J. Electroanal. Chem.* **1996**, *415*(1–2), 197.
- [47] J. Y. Yin, X. Xu, S. Jiang, H. H. Wu, L. Wei, Y. D. Li, J. P. He, K. Xi, Y. F. Gao, *Chem. Eng. J.* **2022**, *431*, 133352.
- [48] L. Edman, *J. Phys. Chem. B* **2000**, *104*(31), 7254.
- [49] D. Sharon, P. Bennington, M. A. Webb, C. T. Deng, J. J. de Pablo, S. N. Patel, P. F. Nealey, *J. Am. Chem. Soc.* **2021**, *143*(8), 3180.
- [50] G. Yang, C. Chanthat, H. Oh, I. A. Ayhan, Q. Wang, *J. Mater. Chem. A* **2017**, *5*(34), 18012.
- [51] N. Chen, Y. J. Dai, Y. Xing, L. L. Wang, C. Guo, R. J. Chen, S. J. Guo, F. Wu, *Energy Environ. Sci.* **2017**, *10*(7), 1660.
- [52] N. Wu, P. H. Chien, Y. T. Li, A. Dolocan, H. H. Xu, B. Y. Xu, N. S. Grundish, H. B. Jin, Y. Y. Hu, J. B. Goodenough, *J. Am. Chem. Soc.* **2020**, *142*(5), 2497.
- [53] L. Chen, W. X. Li, L. Z. Fan, C. W. Nan, Q. Zhang, *Adv. Funct. Mater.* **2019**, *29*(28), 1901047.
- [54] A. Nathani, Y. H. Qi, S. K. Varshney, C. S. Sharma, *Sensor. Actuat. B-Chem* **2022**, *354*, 131240.
- [55] J. Zhang, R. A. Lucas, Y. L. Gu, Y. X. Yang, K. P. Sun, H. B. Li, *Anal. Chem.* **2021**, *93*(13), 5430.
- [56] C. J. Brumlik, C. R. Martin, K. Tokuda, *Anal. Chem.* **1992**, *64*(10), 1201.
- [57] J. Li, H. Luo, K. K. Liu, J. X. Zhang, H. Y. Zhai, X. L. Su, J. S. Wu, X. F. Tang, G. J. Tan, *ACS Appl. Mater. Interfaces* **2023**, *15* (5), 7165.
- [58] J. M. Su, X. Huang, Z. Song, T. P. Xiu, M. E. Badding, J. Jin, Z. Y. Wen, *Ceram. Int.* **2019**, *45*(12), 14991.
- [59] F. Aguesse, W. Manalastas, L. Buannic, J. M. L. del Amo, G. Singh, A. Llordes, J. Kilner, *ACS Appl. Mater. Interfaces* **2017**, *9*(4), 3808.
- [60] E. Y. Yi, W. M. Wang, J. Kieffer, R. M. Laine, *J. Power Sources* **2017**, *352*, 156.
- [61] S. Afyon, F. Krumeich, J. L. M. Rupp, *J. Mater. Chem. A* **2015**, *3*(36), 18636.

Manuscript received: February 1, 2024

Revised manuscript received: March 23, 2024

Accepted manuscript online: April 2, 2024

Version of record online: April 22, 2024